Available online at www.sciencedirect.com

Chemical Engineering Research and Design

journal homepage: www.elsevier.com/locate/cherd

Hydrodynamics, power consumption and bubble size distribution in gas-liquid stirred tanks

*Francesco Maluta, Federico Alberini, Alessandro Paglianti, Giuseppina Montante**

Dipartimento di Chimica Industriale "Toso Montanari", Alma Mater Studiorum Università di Bologna, viale Risorgimento 4, 40136 Bologna, Italy

ARTICLE INFO

Article history:
Received 25 March 2023
Received in revised form 26 April 2023
Accepted 2 May 2023
Available online 5 May 2023

Keywords:
Bubble size distribution
Gassed power consumption
Gas cavities
Gas-liquid flow regime
Computational fluid dynamics
Population balance model

ABSTRACT

In this work, we present the results collected in a gas-liquid stirred tank by a combination of experimental and computational methods, with the aim of presenting original data on the bubbles size distribution and contributing to the development of fully predictive methods for the design and the scale-up of chemical and biochemical gas-liquid reactors. Basic variables which affect mass transfer and consequently the performances of industrial aerobic fermentations are discussed, with special focus on the bubble size distribution, the gassed power consumption and the gas cavities. The current developments of Two Fluid and Population Balance models for obtaining fully predictive results on gas-liquid mixing in stirred tanks are discussed. The results confirm that the correct prediction of the bubble size in the impeller zone is a crucial prerequisite for obtaining reliable results of the hydrodynamics of aerated stirred tanks.

1. Introduction

Gas sparged stirred tanks have been extensively studied in the last decades due to their flexibility and good performance for mass and heat transfer (Middleton and Smith, 2004). Early studies focused on the gas-liquid hydrodynamics, such as the characterization of flow patterns, which started with the analysis of the recirculation ratio (Van't Riet, 1976; Nienow and Lilly, 1979) and successively with the definition of the different flow regimes in aerated tanks stirred with radial impellers (Nienow et al., 1977; Warmoeskerken and Smith, 1986). Early research was also directed in predicting the gassed power consumption (Nienow and Lilly, 1979; Smith et al., 1987), revealing the central role of the aerated cavities forming behind the flat blades of radial and mixed flow impellers in the power reduction mechanism (Bruijn et al., 1974; Takahashi and Nienow, 1992). The pioneering research on sparged gas-liquid tanks also focused on the liquid mixing time, revealing the so-called compartmentalization when multiple radial impellers were used (Manikowski et al., 2009; Pinelli et al., 2001). These studies were primarily experimental, with some initial modeling efforts to understand the flow dynamics. Later on, researchers began investigating the mass transfer mechanisms, providing and comparing techniques to measure the volumetric mass transfer coefficient (Chapman et al., 1982; Linek et al., 1982; Vasconcelos et al., 1997) and the gas hold-up (Hassan and Robinson, 1977; Manikowski et al., 2009; Smith et al., 1977), which are crucial for characterizing gas-liquid mass transfer. One of the best summaries regarding the hydrodynamics of stirred bioreactors is provided by Prof. Alvin W. Nienow (Nienow, 1998).

In recent years, there has been a growing interest in the development of computational models for gas-liquid stirred tanks (Middleton and Smith, 2004), which may contribute to a more comprehensive understanding of the complex flow patterns and mixing dynamics. This computational development and the availability of more advanced experimental techniques allowed not only to characterize the global behavior of aerated stirred tanks, but also to obtain local

* Corresponding author.
E-mail address: giuseppina.montante@unibo.it (G. Montante).
https://doi.org/10.1016/j.cherd.2023.05.006

Nomenclature

List of symbols

a	Coalescence frequency – 1/s.
B_B^B	Bubble birth rate due to breakage – 1/s.
B_B^C	Bubble birth rate due to coalescence – 1/s.
C	Impeller off-bottom clearance – m.
C_1	Terminal velocity constant.
C_2, C_3, C_4	Laakkonen et al. breakup kernel parameters.
C_5	Coulaloglou and Tavlarides coalescence kernel parameter.
d	Daughter bubble size – m.
d'	Mother bubble size – m.
d_{10}	Numerical mean diameter – m.
d_{32}	Sauter mean diameter – m.
d_{32}^{Bulk}	Sauter mean diameter in the bulk – m.
$d_{32}^{Impeller}$	Sauter mean diameter in the impeller zone – m.
d_{BO}	Bubble size exiting the sparger – m.
d_O	Ring sparger hole diameter – m.
D	Impeller diameter – m.
D_B^B	Bubble death rate due to breakage – 1/s.
D_B^C	Bubble death rate due to coalescence – 1/s.
Eo	Eötvös number.
$\mathbf{)}'$	Drag force – N/m^3.
Fl_G	Flow number.
Fr	Froude number.
$\mathbf{)}_7'$	Turbulent dispersion force – N/m^3.
g	Gravitational acceleration – m/s^2.
$g(d)$	Bubble breakup frequency – 1/s.
H	Tank height – m.
H_L	Liquid height – m.
i_{max}	Maximum pixel intensity.
i_{min}	Minimum pixel intensity.
k	Turbulent kinetic energy – m^2/s^2.
l_x	Pixel intensity local threshold.
Mo	Morton number.
n	Bubble number density function.
N	Impeller rotational speed – rps.
Np	Impeller power number.
P	Pressure – Pa.
P_g	Gassed power consumption – W.
P_u	Ungassed power consumption – W.
Q_G	Gas flow rate – m^3/s.
Re	Impeller Reynolds number.
Re_B	Bubble Reynolds number.
Re_O	Orifice Reynolds number.
T	Tank diameter – m.
$\mathbf{x}_\cdot$	Gas phase velocity – m/s.
$\mathbf{x}_i$	i-th phase velocity – m/s.
$\mathbf{x}_y$	Liquid phase velocity – m/s.
U_t	Bubble terminal velocity – m/s.
V_I	Impeller swept volume – m^3.
z	Axial coordinate – m.
α_G	Gas phase volume fraction.
α_i	i-th phase volume fraction.
α_L	Liquid phase volume fraction.
β	Terminal velocity constant.
$\beta(d, d')$	daughter distribution function.
Δ_{EXP}	Percent deviation of the numerical d from the experimental d.
ε	Turbulent dissipation rate – m^2/s^3.
ε_{RE}	Richardson extrapolation of ε – m^2/s^3.
ε_{RE}^*	Dimensionless ε_{RE}.
$\eta(d, d')$	Coalescence efficiency.
μ_L	Liquid viscosity – Pa·s.
μ_t	Eddy viscosity – Pa·s.
ρ_G	Gas density – kg/m^3.
ρ_i	i-th phase density – kg/m^3.
ρ_{mix}	Mixture density – kg/m^3.
ρ_L	Liquid density – kg/m^3.
σ	Air-water interfacial tension – N/m.
$\sigma_{t,L}$	Eddy viscosity Prandtl number.
$\boldsymbol{\tau_I}$	Viscous stress tensor – N/m^2.
$\boldsymbol{\tau_L^\vee}$	Reynolds stress tensor – N/m^2.

Acronyms

BSD	Bubble Size Distribution.
CFD	Computational Fluid Dynamics.
DDF	Daughter Distribution Function.
PBM	Population Balance Model.
PDF	Probability Density Function.
QMOM	Quadrature Method Of Moments.
RANS	Reynolds Averaged Navier-Stokes equations.
RPD	Relative Power Demand.
TFM	Two-Fluid Model.

information on the turbulent fluid dynamic characteristics under gassed conditions (Aubin et al., 2004). In addition, it became possible to experimentally measure the local bubble size distribution. One of the first studies adopted a photographic technique to obtain the bubble size distribution close to the impeller at low aeration rates of 0.01–0.025vvm (Takahashi et al., 1992). Later studies slightly increased the aeration rate up to about 0.07vvm, measuring the bubble size distribution in the bulk of the aerated vessel with digital imaging techniques (Montante et al., 2008), Laser-Induced Fluorescence with ShadowAnalysis (Busciglio et al., 2013), and multiple techniques consisting of digital imaging, capillary suction, and phase doppler anemometry (Laakkonen et al., 2005). Studies at higher gas flow rates, 0.2–0.5 vvm, were conducted both with a capillary suction technique (Alves et al., 2002) and with photographic techniques (Kálal et al., 2014a), providing the Sauter mean diameter in several tank zones. Despite the high accuracy, relevance and breath of these studies, the aeration rates investigated are lower than those typically adopted in fermentation processes (Nienow, 1990), and research is needed to provide data exploitable in industrial operations.

Alongside these experimental works, predictive approaches based on computational fluid dynamics (CFD) simulations and coupling with population balance models (PBM) have started being applied from the '90 s (Bakker and Van den Akker, 1994; Venneker et al., 2002). The central role of the bubble size in predicting the overall behavior of the gas dispersion has been known for a long time (Sideman et al., 1966). To this end, a great deal of work has been done in developing specific models to describe the evolution of the size of the bubbles in aerated stirred tanks, and in turbulent dispersion in general. These models, or kernels, combine physical insight on the mechanisms governing breakup and coalescence rate with empirical observations. From early correlations in which instantaneous coalescence was obtained after sufficiently energetic collisions (Howarth, 1964) and correlations in which complex concept from chemical-reaction kinetics were applied to bubble breakup (Ross and

Curl, 1973), coalescence and breakup kernels evolved to model bubble aggregation by describing the inter-bubble film with deformable bubble surfaces through a multifractal approach to (Podgórska and Bałdyga, 2001) and to breakup rates derived by considering the entire cascade of turbulence (Niño et al., 2020). Comprehensive reviews of the breakup and coalescence kernels may be found in the literature (Liao and Lucas, 2010, 2009; Solsvik et al., 2013).

In 2004, in the Handbook of Industrial Mixing, Middleton and Smith stated that open questions regarding the CFD simulations of sparged stirred tanks concerned the accurate description of the local turbulence in multiphase flows, the breakup and coalescence of bubbles, and the prediction of the gas cavities (Middleton and Smith, 2004). Regarding the first issue, fundamental investigation is still needed to address turbulence modulation, preferential concentration of bubbles and interphase coupling models (Balachandar and Eaton, 2010). As stated above, several models to describe breakup and coalescence of bubbles are available, their adoption in CFD codes is widespread, but testing in different applications and operative conditions, validation with larger dataset and improvement in the understanding of the physics behind coalescence and breakup phenomena is still needed (Liao and Lucas, 2010, 2009). The last issue pointed by Middleton and Smith was recently addressed, since the aerated cavities behind the blades of the impeller were obtained by a fully predictive modelling approach (Cappello et al., 2021; Maluta et al., 2021c). One of the key aspects to reliably predict the shape and size of the aerated cavities and, consequentially, the gas-liquid flow regimes and relative power demand is to correctly predict the bubble size in the impeller zone (Maluta et al., 2021d). It is no surprising that the importance of the gas-liquid flow in the impeller region on the gas-dispersion in aerated stirred tanks was already recognized more than 30 years ago by Prof. Alvin Nienow (Takahashi and Nienow, 1992). In the words of Prof. Matthias Kraume at the 2021 Awards Ceremony of the EFCE Working Party on Mixing: “Wherever you go, you will probably find out Alvin has been there”.

The present work analyzes an aerated stirred tank operating at gas flow rates and power consumptions typically adopted in fermenter operations (Nienow, 1990). Original experimental data on the bubble size distribution in two different tank zones, the shape and size of the aerated cavities, the power consumption, and the gas phase distribution in the tank are presented. The experimental results are used to benchmark the numerical predictions obtained by coupling the flow equations with a PBM, adopting breakup and coalescence kernels selected from the literature. The goal is to assess the behavior of some of most commonly adopted kernels in operative conditions which are adopted in industrial applications.

In the following, firstly the system is described in detail, and the experimental methods used to characterize the bubble size distribution, the power consumption and the gas-liquid fluid dynamics are presented. Successively, the computational model for the CFD simulation of the experimentally characterized stirred tank is described, together with the numerical methods adopted for its solution. The results are then shown and discussed, in terms of bubble size distribution, aerated cavities, relative power demand and gas distribution. Lastly, conclusions are drawn.

2. The aerated stirred tank and experimental techniques

2.1. The system

The stirred tank considered in this work is a flat bottom cylindrical tank of diameter T = 0.232 m and height H= 2 T. The ungassed water (density ρ_L = 998 kg/m^3 and viscosity μ_L = 0.001 Pa·s) height is equal to H_L= 1.4 T and agitation is provided by a Rushton impeller with diameter D=T/3, positioned at an off-bottom clearance of C=T/2. Four baffles of width equal to T/10 are positioned on the walls of the tank 90° apart. A ring sparger of diameter T/5 positioned at an off-bottom distance of 0.25 T injects air (ρ_G = 1.225 kg/m^3) into the system, through 36 holes 1 mm in diameter, d_O, on its upper side.

One operative condition was studied, in which the impeller rotational speed, N, was equal to 433 rpm and the volumetric gas flow rate, Q_G, was equal to 10 L/min. The resulting aeration is equal to 0.728 vvm, with a superficial gas velocity of 0.0039 m/s and the resulting flow, Fl_G, Froude, *Fr*, and Reynolds, *Re* numbers equal to:

$$Fl_G = Q_G/ND^3 = 0.05 \quad (1)$$

$$Fr = N^2D/g = 0.41 \quad (2)$$

$$\mathrm{Re} = ND^2\rho_L/\mu_L \approx 43,000 \quad (3)$$

With *g* being the gravitational acceleration. Based on the correlations developed by Nienow for aerated stirred tanks (Nienow, 1998), the expected impeller flow regime is loading, with the presence of small ‘3–3’ cavities forming behind the blades of the impeller and the tank is in fully turbulent regime.

2.2. Experimental techniques

In the following, details of the techniques adopted for the measurement of the bubble size distribution (BSD) and of the power consumption are provided. In addition, cavities were detected by positioning a dimmable LED panel (40 W, 4000 lumen) on top of the tank and capturing pictures of the bottom of the vessel through a mirror positioned at 45° with respect to the horizontal. Pictures were obtained by lowering the camera shutter speed to 1/1000 s, a focal length of 5.4 mm and a ratio of the aperture to the focal length equal to f/1.8. Also, the gas distribution in the vessel was qualitatively captured by backlighting the vessel with the light source dimmed to its minimum and increasing the shutter speed to 0.5 s. The overall gas hold-up measurement was renounced since at the selected gas flow rate, which ensures good optical access for the BSD, the variation of the height of the free-liquid surface was of just few millimeters.

2.2.1. The bubble size measurements

The experimental set up for the measurements of the bubble distributions consists of a camera, Phantom VEO E340L, connected with a synchronizer and a Litron Dual-Power 50–50 laser. On the laser head a coupler was mounted to connect one end of a fiber optic light guide. The other end was connected to a ShadowStrobe, provided by Dantec. The ShadowStrobe consists of front lens mounted on a post

holder and an adjustable internal housing (behind the front lens) which enables the tuning of the light cone of the strobe. The power of the laser was adjusted to provide a homogenous background and an average grey scale value around 2000 to avoid any pixel saturation.

Measurements were performed in two sampling zones. Both sampling zones correspond to a circle of diameter equal to 5 cm located approximately mid-way between two baffles with the camera focus set on the walls of the tank. The centre of the lower sampling zone was located at an axial coordinate, z, of 0.172 m from the vessel bottom(z/T = 0.74), while the upper sampling zone was at an axial coordinate of 0.241 m (z/T = 1.04). Lower elevations were not investigated due to optical limitations in the impeller discharge zone and negligible bubble number below the impeller. 500 images were collected in each sampling zone with a time interval of 0.1 s between two consecutive acquisitions.

The bubble images were post-processed with the Adaptive Shadow Tracking method (Dantec Dynamics, 2022; Wang et al., 2017), as implemented in the DynamicStudio 7.6 software. The method is based on the detection and measurement of the shadows generated by the bubbles from the back light pointing at the camera. With the selected instrumentation, the back illumination was uniform, and the image post processing did not require any filtering procedure. The out-of-focus bubbles were not analyzed. Images were preprocessed with a denoised algorithm, which reduces the random Gaussian noise, while preserving the shape and gradient of the images, with the intensity of this filter set to its maximum value. For the optimization of the bubble detection, each particle is segmented from the global image introducing a variable interrogation window in which only a single bubble is present. The size of the interrogation window directly changes the sensitivity towards small or large particles. The threshold value for the detection algorithm ranges from – 8 to + 8. With the camera set-up adopted in this work, the threshold value of 3 corresponded to the sharpest gradients (i.e., bubbles on focus on the detection plane) and larger values to more blurred gradients, hence detecting more out-of-focus bubbles. Therefore, the threshold value of 3 was adopted, thus excluding out-of-focus shadows. Once bubbles are detected through the procedure described above, a bounding box centred on the detected particle is drawn and the bubble is segmented. Inside each and every bounding box, the boundaries of the bubbles are detected from the analysis of the intensity of the gradient normalized with the maximum, i_{max}, and minimum, i_{min}, pixel intensity values inside the bounding box. The local threshold level, l_x, is thus defined as:

$$l_x = i_{min} + (i_{max} - i_{min}) \times \frac{x}{100} \tag{4}$$

The value of x suggested by Fdida and Blaisot (Fdida and Blaisot, 2010) for perfectly circular objects was 61, and in the present work a value of x = 40 with a confidence interval of ± 5% has been identified to maximize the number of bubbles identified. Clearly, the value of l_x depends on the size of the bounding box, and larger bounding boxes allow to increase the difference between i_{max} and i_{min}, provided that neighbor bubbles do not enter multiple bounding boxes. A value of 125% the size of the box drawn by the automatic detection algorithm was selected as a good compromise between resolution and accuracy. Ultimately, to remove measurement errors due to bubble overlapping and bubble shadows on multiple depth, a validation procedure was applied. In particular, bubbles with diameters between 0.1 mm (camera detection limit) and 6 mm (based on the maximum size of individual bubbles detected manually) were retained, while the rest were discarded. In addition, bubbles with eccentricity lower than 0.5 were also disregarded, being the eccentricity defined as the ratio between the minor axis over the major axis. It was observed that eccentricities lower than 0.5 were associated with overlapping bubbles. A sensitivity study on each of the parameters needed to detect and measure the bubbles was performed, finding a relatively good robustness of the algorithm. The most influential parameters affecting the bubble population were the maximum and minimum bubble size, but these parameters were also the easiest to set, by visual estimation of the largest and smallest bubbles. Once the bubbles in an image were recognized by the algorithm, all the images were processed, and the bubble population was obtained.

2.2.2. *The power consumption measurements*

The power consumption was obtained by measuring the torque on the shaft by using the Kistler torque sensor type 4502A2RA, which is based on a strain gauges system. The sensor was mounted below the electrical motor, between the motor head and the metal shaft combining the two parts with couplings and adapters. The sensor has a rated torque of 2 Nm, a maximum torque of 1.5 the rated one and an accuracy class of 0.2. A measurement of the torque due to friction dissipation was performed with the rotating shaft in the empty vessel. Such torque is subtracted from the measured one with the single-phase system and also for the aerated system as well.

The power transferred by the shaft to the fluid through the impeller, P, was calculated as the net torque (measured torque minus the friction torque) times the impeller speed.

3. Computational model

3.1. *Gas-liquid fluid dynamics*

The computational model adopted in the present study is based on the solution of the steady state, isothermal, incompressible Reynolds Averaged Navier Stokes (RANS) equations, extended to two phases with the so-called Two-Fluid model (TFM), and for the i-th phase they read as:

$$\nabla\cdot(\alpha_i\rho_i\mathbf{X_I}) = 0 \tag{5}$$

$$\nabla\cdot(\alpha_i\rho_i\mathbf{X_I}\mathbf{X_I}) = -\alpha_i\nabla P + \alpha_i\rho_i\mathbf{J} + \nabla\cdot(\tau_L + \tau_L^{W}) +)' +)_{7'} \tag{6}$$

Where α_i is the volume fraction of the phase i, ρ_i is its density and $\mathbf{X_I}$ its velocity. The pressure shared by the two phases is indicated as P, $\mathbf{J}$ is the gravitational acceleration. The terms τ_I and τ_L^{ν} are, respectively, the viscous and Reynolds stress tensor, and the latter was closed with the multiphase $k-\varepsilon$ turbulence model extended to multiphase systems with the so-called mixture model, adopting the properties of the mixture as reported in the literature for similar systems (Buffo et al., 2012; Petitti et al., 2010). The interphase forces considered are the drag, $)'$, and the turbulent dispersion force, $)_{7'}$.

The drag and the turbulent dispersion forces were expressed in terms of the bubble terminal velocity, U_t (Scargiali et al., 2007; Maluta et al., 2021d) and both the gas and liquid volume fractions are included arising from

considering the force balance in an Eulerian frame (Simonnet et al., 2007; Maluta et al., 2021c). The drag force reads as:

$$)' = \frac{\alpha_L \alpha_G}{U_t^2} g(\rho_L - \rho_G) \| \mathbf{X}_* - \mathbf{X}_/ \| (\mathbf{X}_* - \mathbf{X}_/) \quad (7)$$

With the bubble terminal velocity, U_t, is obtained with the correlation by Grace (Clift et al., 2005):

$$U_t = \frac{\mu_L}{\rho_L d_{32}} Mo^{-0.149} \left(C_1 \left[\frac{4}{3} \quad Eo \quad Mo^{-0.149} \right]^{\beta} - 0.857 \right) \quad (8)$$

Where d_{32} is the bubble Sauter mean diameter, and the Morton, $Mo = \mu_L^4 g(\rho_L - \rho_G)/(\rho_L^2 \sigma^3)$, and the Eötvös number, $Eo = g(\rho_L - \rho_G) d_{32}^2/\sigma$, depend on the air-water interfacial tension, $\sigma = 0.072$ N/m. The parameters C_1 and β become 0.94 and 0.757 respectively, when the term in square brackets assumes values between 2 and 59.3, while when it is larger than 59.3 C_1 and β are equal to 3.42 and 0.441. The Grace correlation strictly applies to ellipsoidal bubbles, but it can also be applied to spherical bubbles up to bubbles Reynolds number, $Re_B = U_t \rho_L d_{32}/\mu_L$, of 400, being the deviation between the terminal velocity obtained with the Schiller and Naumann correlation and the Grace correlation less than 5% (Maluta et al., 2021c). Due to the uncertainties of both the effects of the disperse phase volume fraction and of the free stream turbulence on the drag force, in this work Eq.(8) is adopted without including any correction.

The turbulent dispersion force is described with the model by Burns (Burns et al., 2004), and it reads:

$$)_7' = \frac{\alpha_L \alpha_G}{U_t^2} g(\rho_L - \rho_G) \| \mathbf{X}_* - \mathbf{X}_/ \| \left[\frac{\mu_t}{\rho_L \sigma_{t,L}} \left(\frac{\nabla \alpha_G}{\alpha_G} - \frac{\nabla \alpha_L}{\alpha_L} \right) \right] \quad (9)$$

With $\sigma_{t,L}$ being the eddy viscosity Prandtl number, assuming a value of 0.9 and μ_t being the eddy viscosity calculated as:

$$\mu_t = 0.09 \rho_{mix} k^2/\varepsilon \quad (10)$$

With ρ_{mix} being the density of the mixture and k and ε being the turbulent kinetic energy and its dissipation rate, respectively, and they are the transported variables of the turbulence model.

3.2. Population balance model

In order to close the set of equations presented in Section 3.1, the bubble Sauter mean diameter must be provided. In this work, an initial gas-liquid flow field was calculated by assuming a constant bubble size representative of the bubble diameter expected in the impeller zone, as proposed in previous works (Maluta et al., 2022b, 2021d). It was demonstrated that adopting the bubble size in the impeller zone produces good agreement with correlations from the literature and experimental data, in terms of cavities shape and size, relative power demand, gas hold-up, gas distribution and, to some extent, k_La predictions (Maluta et al., 2022c, 2021d). The modelling approach was tested in different operative conditions, tank scales and multiple impellers (Maluta et al., 2022a, 2021c).

A workflow for the simulation of aerated gas-liquid stirred tanks was previously proposed, based on obtaining the gas-liquid flow field with a first guess bubble size from available correlations (Maluta et al., 2022b). The preliminary evaluation of the bubble terminal velocity obtained with a decoupled solution of the PBM was not performed, since the objective of this work is the direct comparison of the bubble size distribution and the resulting fluid dynamics from the simulations with experimental measurement. Therefore, just the first part of the proposed workflow was followed, meaning that the correlation developed by Alves et al. (Alves et al., 2002) was adopted to obtain the first guess bubble size in the impeller zone, and for coalescing systems it reads as:

$$d_{32} = 8.5 \left(1 + 32.5 \frac{Q_G}{D^2} \right) \left(\frac{P_g}{V_I} \right)^{-0.24} \quad (11)$$

Where the gassed power consumption, Pg, is divided by the volume swept by the blades of the impeller, $V_I = \pi D^3/20$. The resulting Sauter mean diameter in the impeller zone in the operative conditions considered is equal to 1.28 mm.

Successively, a population balance model, PBM, was solved to obtain the local d_{32} in the tank. The PBM reads as:

$$\nabla \cdot (\mathbf{X}_* n) = B_B^B + B_B^C - D_B^B - D_B^C \quad (12)$$

With n being the bubble number density function, and the terms on the right-hand side of Eq. (12) are birth, B_B, and death, D_B, rates due to the discrete events associated with the breakup, B, and the coalescence, C, of the bubbles.

The bubble birth rate of a bubble of diameter d due to the breakup of bubbles with diameter d' and the death rate due to breakup of a bubble of diameter d read, respectively as:

$$B_B^B(d) = \int_d^{\infty} \beta(d, d') g(d') n(d) \, dd' \quad (13)$$

$$D_B^B(d) = g(d) n(d) \quad (14)$$

Where the breakup frequency, $g(d')$, and the daughter distribution function $\beta(d, d')$ are described either with the model by Laakkonen et al. (Laakkonen et al., 2006) or the one by Lehr et al. (Lehr et al., 2002). These two different models were adopted to describe the breakup source terms since they are frequently adopted in the open literature to describe gas-liquid distributions in stirred tanks (Buffo et al., 2012; Kálal et al., 2014b; Laakkonen et al., 2007; Maluta et al., 2022a) and because analytical solutions for the daughter distribution function and breakup frequency exist, which simplifies their implementation. Solsvik and Jakobsen (Solsvik and Jakobsen, 2015) studied the breakup of a single bubble in a tank stirred with a Rushton turbine at different impeller rotational speeds and found that the probability of binary breakage decreases as the impeller rotational speed increases. Since most of the breakup events happen close to the impeller (Maluta et al., 2021a; Vonka and Soos, 2015), the results by Solsvik and Jakobsen were regressed based on the mean turbulent dissipation rate in the impeller zone and for the operative conditions considered in this work it was found that around 65% of the breakup events would result in binary breakage. Similar conclusions were obtained with a regression based on the work by Hasan (2017). For these reasons, just binary breakage was considered in this work. The adoption of different fragment numbers and daughter distribution functions must satisfy the conditions that the moment of order zero of the daughter distribution function equals the number of fragments, and that the third moment of the daughter distribution function is equal to the mother bubble volume. Future work may be addressed to studying different daughter distribution functions and a different number of fragments, as previously done for liquid-liquid systems (Maluta et al., 2021b).

The breakup frequency of Laakkonen and Lehr are expressed respectively as:

$$g(d) = C_2\varepsilon^{1/3}erfc\left(\sqrt{C_3\frac{\sigma}{\rho_L\varepsilon^{2/3}d^{5/3}} + C_4\frac{\mu_L}{\sqrt{\rho_L\rho_G}\varepsilon^{1/3}d^{4/3}}}\right) \quad (15)$$

$$g(d) = \frac{1}{2}\frac{d^{\frac{5}{3}}\varepsilon^{\frac{19}{15}}\rho_L^{\frac{7}{5}}}{\sigma^{\frac{7}{5}}}\exp\left(-\frac{\sqrt{2}\sigma^{\frac{9}{5}}}{d^3\rho_L^{\frac{9}{5}}\varepsilon^{\frac{6}{5}}}\right) \quad (16)$$

Where the empirical constants in the model by Laakkonen are equal to $C_2 = 6.0$ (Petitti et al., 2010), $C_3 = 0.04$ and $C_4 = 0.01$ (Laakkonen et al., 2006).

The analytic integral of the daughter size distribution functions proposed by Laakkonen and Lehr are, respectively:

$$\beta(d, d') = 180\left(\frac{d^2}{d'^3}\right)\left(\frac{d^3}{d'^3}\right)^2\left(1 - \frac{d^3}{d'^3}\right)^2 \quad (17)$$

$$\beta(d, d') = \begin{cases} \dfrac{9d^2}{\sqrt{\pi}d'^3}\dfrac{\exp\left\{-\frac{9}{4}\left[\ln\left(\frac{2^{\frac{2}{5}}d_\rho^{\frac{3}{5}}\varepsilon^{\frac{2}{5}}}{\sigma^{\frac{3}{5}}}\right)\right]^2\right\}}{\left\{1 + erf\left[\frac{3}{2}\ln\left(\frac{\frac{1}{2^{15}}d'^{\frac{3}{5}}\rho_L^{\frac{3}{5}}\varepsilon^{\frac{2}{5}}}{\sigma^{\frac{3}{5}}}\right)\right]\right\}}, for 0 < d \le d'/2^{\frac{1}{3}} \\ \beta\left((d'^3 - d^3)^{\frac{1}{3}}, d'\right), for d'/2^{\frac{1}{3}} < d < d' \end{cases} \quad (18)$$

The daughter distribution function proposed by Laakkonen is based on a beta distribution, in which symmetric breakup is considered as the event with the highest probability, resulting in a bell shape. The daughter distribution proposed by Lehr assumes a bell shape for small bubbles, resulting in symmetric breakup. Since the model assumes that breakage occurs when the kinetic energy of an eddy impacting a bubble is higher than the interfacial energy of the smallest daughter bubble, small eddies in a low turbulence environment are not energetic enough to split off small bubbles from the parent one, while large eddies might succeed. Therefore, in these conditions equal-sized breakup is the most probable. On the other hand, for large bubbles and highly turbulent flows the number of highly energetic small eddies increases, causing the daughter distribution function to change to a bimodal breakage, where one smaller and one larger bubble are produced, thus assuming a M-shape (Kálal et al., 2014a; Lehr et al., 2002). In this work, together with the breakup model proposed by Laakkonen and Lehr, a combination of the two was tested, in which the breakup frequency is given by the model by Laakkonen, Eq. (15), and the daughter distribution function by Lehr, Eq. (18), was assumed.

The bubble birth rate and the death rate due to coalescence read, respectively as:

$$B_B^C(d) = \frac{1}{2}\int_0^d a\left((d^3 - d'^3)^{1/3}, d'\right)n(d)n\left((d^3 - d'^3)^{1/3}\right)dd' \quad (19)$$

$$D_B^C(d) = \int_0^\infty a(d, d')n(d)n(d')dd' \quad (20)$$

With a being the coalescence frequency, which was described with the model proposed by Coulaloglou and Tavlarides (Coulaloglou and Tavlarides, 1977) with an algebraic correction (Prince and Blanch, 1990), as done in several studies on similar systems (Maluta et al., 2022a, 2022b; Petitti et al., 2013, 2010). The coalescence frequency is equal to:

$$a(d, d') = 0.88\varepsilon^{1/3}(d + d')^2\left(d^{2/3} + d'^{2/3}\right)^{1/2}\eta(d, d') \quad (21)$$

Where the coalescence efficiency of two colliding bubbles is expressed as:

$$\eta(d, d') = \exp\left(-C_5\frac{\mu_L\rho_L\varepsilon}{\sigma^2}\left(\frac{d\,d'}{d + d'}\right)^4\right) \quad (22)$$

With the empirical constant $C_5 = 6 \times 10^9$ containing information on the initial and final liquid film critical thickness between the colliding bubbles (Petitti et al., 2010).

The PBM presented was solved with the Quadrature Method of Moments, as already done for similar systems (Buffo et al., 2016, 2013; Buffo and Marchisio, 2014), by simplifying the number density function with a quadrature approximation and applying a moment transform to Eq. (12), thus obtaining the transport equations for the moments of the bubble number density function (Marchisio and Fox, 2013). Three quadrature abscissas and weights were obtained from the first six moments of the distribution with the well-known Product-Difference algorithm.

4. Numerical methods

The model equations presented in Section 3 were solved in ANSYS Fluent 2020 R2, in a computational domain matching the experimental tank described in Section 2.1. Two heights of the domain were considered, one corresponding to the total height of the tank, equal to 2 T and one corresponding to the liquid height equal to 1.4 T. The domain is constituted by 1.2 million cells in the first case, as shown in Figs. 1, and 1 million cells in the latter. As already done in a previous study, the computational mesh was selectively refined in the impeller zone since it was demonstrated that this refinement allows to obtain results as accurate as more dense grids (Maluta et al., 2022c). On the solid walls of the tank no-slip boundary conditions were enforced for both fluids, except for the upper part of the air sparger, where a velocity inlet for the gas phase was defined. In the domain with H= 2 T on the top surface of the tank a pressure outlet was defined with a zero-gauge pressure, while in the domain with H= 1.4 T a degassing boundary condition was defined on the top surface, which acts as a mass sink for the gas phase and a free-slip boundary condition for the liquid phase. The initial condition of the simulations was that of the vessel filled with the ungassed still liquid up to H_L= 1.4 T. In the case of the taller vessel, the computational domain was filled with air from the height of 1.4–2 T. No additional models were implemented to describe the free liquid surface and the gas space. The same approach was applied to describe the fluid dynamics of a dual impeller vortex ingesting stirred tank (Maluta et al., 2019).

The motion of the impeller was described with the multiple reference frame approach. A pseudo-transient solver was adopted to solve the discretized equations of the model, with a pseudo time step of 0.001 s. The momentum conservation equations and the transport equations of the turbulent variables were discretized with a second order UPWIND scheme, and the volume fraction transport equations were discretized with the QUICK scheme. The pressure-based coupled algorithm was adopted to couple the pressure and velocity equations. The adopted numerical set-up was validated in previous works, and it proved robust for the solution of the gas-liquid fluid dynamics equations (Maluta et al., 2022a, 2021c, 2021d).

Concerning the solution of the PBM, a zero-flux boundary condition was defined on the solid walls of the domain, except for the upper part of the air sparger. On this surface a delta distribution centered on the size of the bubbles exiting

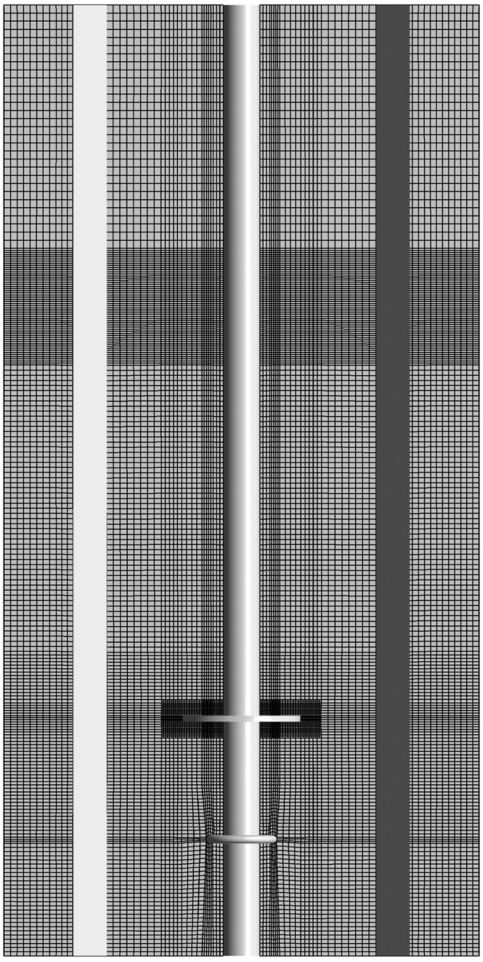

Fig. 1 – Tank geometry (H=2 T) with the domain discretization shown on a vertical plane midway between two consecutive baffles.

the sparger, d_{BO}, was defined. At high gas flow rate, when the orifice Reynolds number, $Re_O = 4Q_G\rho_G/\pi d_O\mu_G$, is higher than 2000 jetting from the holes of the sparger is expected. In the operative conditions studied in this work, the orifice Reynolds number is about 15,000 and the following correlation for the bubble size can be adopted (Leibson et al., 1956):

$$d_{BO} = 0.0071Re_O^{-0.05} \quad (23)$$

Which gives a size of the bubble exiting the sparger equal to 4.4 mm.

The moment transport equations were discretized with a second order UPWIND scheme.

5. Results

In this section, firstly the experimental bubble size distributions measured in the two sampling zones described in Section 2 are presented, together with the shape of the aerated cavities forming behind the flat blades of the Rushton impeller, the impeller power consumption, and the qualitative gas distribution in the tank. Then, the results of the different models are presented and compared against the experimental data. The effect of the breakup models on the local fluid dynamics is also analyzed.

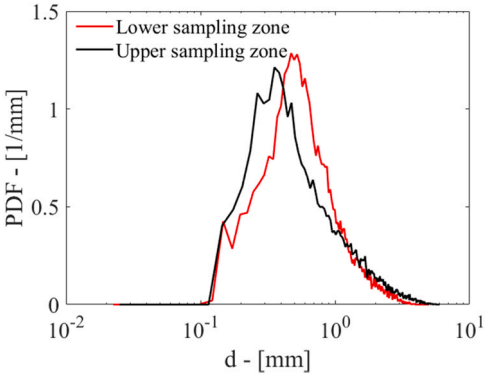

Fig. 2 – Experimentally determined bubble number PDFs in the two different sampling zones.

Table 1 – Experimentally determined bubbles mean diameters.

	d_{10} [mm]	d_{32} [mm]
Lower Sampling Zone	0.88	1.75
Upper Sampling Zone	1.06	2.55

5.1. *Experimental results*

The bubble size distribution was measured from 500 images acquired in single-frame mode, for both the sampling positions considered in this work. From those images, the bubble detection algorithm described in Section 2 allowed to collect more than 13,000 bubbles in the lower position and more than 17,000 in the upper position. In both cases, the number of bubbles analyzed is higher than the threshold of 10,000 suggested by Laakkonen et al. (Laakkonen et al., 2005). The numerical probability density functions, PDFs, were calculated and discretized in 200 bins, with diameters ranging from 0.1 mm to 6.0 mm. The resulting PDFs are shown in Fig. 2.

Fig. 2 shows that similar PDFs are obtained in the two different sampling zones. In both cases bubbles smaller than 0.1 mm were not detected by the camera. In the lower sampling zone, the PDF peaks at around 0.50 mm, while in the upper sampling zone it peaks at 0.35 mm. Despite the position of the peaks, smaller mean diameters are found in the lower sampling zone, as shown in Table 1.

The difference between the position of the peaks and the mean diameters is driven by the number of larger bubbles in the upper position, that shifts the bubble mean diameters towards larger sizes. The results of Table 1 highlight that moving away from the impeller results in higher mean diameters and wider distributions. This behavior is consistent with what observed by Laakkonen et al. (Laakkonen et al., 2005) in similar positions for air-water mixtures. The differences in the bubble size distribution observed in the two sampling zones suggest that coalescence rate has a small but noticeable effect on the bubble population. Comparing the bubble Sauter mean diameter with the correlations developed by Alves et al. (Alves et al., 2002) reveals that the measured d_{32} obtained in the two sampling positions is smaller than the predicted value in the bulk for coalescing systems, $d_{32}^{Bulk} = 3.62$ mm, and higher than the predicted value in the impeller zone, $d_{32}^{Impeller} = 1.29$ mm.

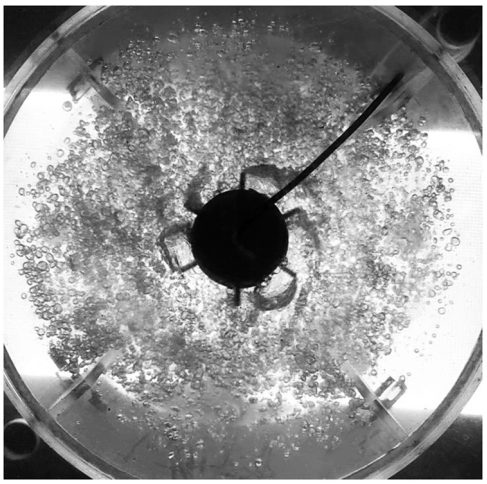

Fig. 3 – '3–3' aerated cavities behind the blades of the Rushton impeller. Impeller rotating in a counter-clockwise direction.

In the operative conditions considered, '3–3' cavities are expected to form behind the blades of the Rushton impeller. Observing the tank from below, the aerated cavities were observed, and they are shown in Fig. 3.

Fig. 3 clearly shows that 3 large cavities are formed behind blades positioned 120° apart, and 3 smaller clinging cavities follow the remaining blades. The shape of the cavities is in agreement with the predictions by Warmoeskerken, Smith and Nienow (Nienow et al., 1985; Warmoeskerken et al., 1981), and the ratio between the projection of the area occupied by the cavities on a plane parallel to the tank bottom and the projection of the area swept by the impeller is equal to 0.36. This value agrees with previous results collected by Paglianti et al. in a similar system (Paglianti et al., 2008).

The formation of aerated cavities behind the impeller blades reduces the impeller power consumption with respect to single phase conditions. The impeller power number, Np, in single phase conditions was experimentally determined from several measurements with impeller speeds ranging from 210 rpm to 560 rpm, giving impeller Reynolds numbers from about 20,000–55,000, corresponding to a stirred tank operating in fully turbulent regime. The impeller power number is equal to 5.16, with a standard deviation of 0.85, and this value was used to calculate the ungassed power consumption, P_u, in the studied operative conditions and it is equal to:

$$P_u = Np \quad \rho_L D^5 N^3 = 5.36W \tag{24}$$

The measured aerated power consumption, P_g, was equal to 2.65 W, and by dividing this value by P_u at the same impeller rotational speed a relative power demand, RPD, of 0.50 was obtained.

The measured RPD value was compared with the available correlations developed by Nienow (Nienow, 1998) for tanks stirred with a Rushton turbine with a liquid height equal to the tank diameter. The correlations predict a RPD of 0.53, which is very close to the measured value. This result certifies once again the invaluable importance of the correlations developed by Prof. Nienow, that still nowadays represent a great asset in the analysis and characterization of aerated stirred tanks.

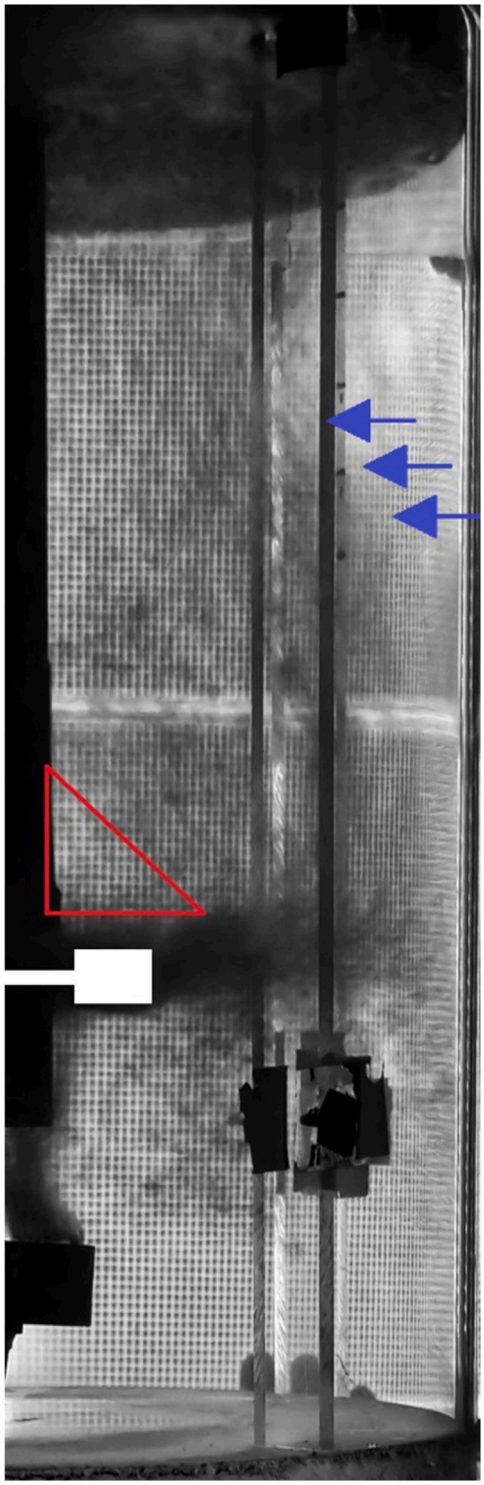

Fig. 4 – Gas distribution inside the tank. In white the outline of the impeller is highlighted, in blue, arrows pointing to the deviation of the vertically rising gas plume moving towards the centre of the tank, and in red the conic zone with lower gas volume fraction above the impeller.

The qualitative gas distribution inside the tank was acquired as described in Section 2, and the acquired image is shown in Fig. 4.

Fig. 4 shows that the gas exiting the sparger reaches the impeller zone, where it is distributed in the volume by the radial jet. The aerated jet forms an angle of around 15° with

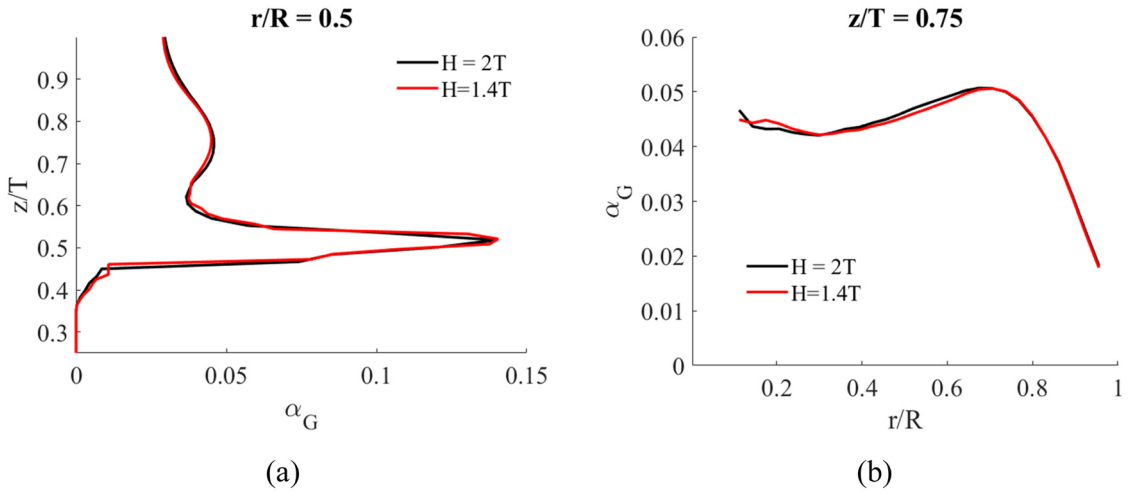

Fig. 5 – Axial (a) and radial (b) gas volume fraction profiles at selected radial and axial coordinates on a vertical plane midway between two consecutive baffles, as predicted by different modelling approaches.

the impeller plane, due to the upward motion of the gas phase. Bubbles are recirculated below the plane of the impeller, up to a distance of around 0.78D below the centre of the Rushton turbine. In the upper part of the tank, at about z/T = 0.97, the bubbles in the vertically rising plume towards the walls of the vessel are drawn towards the centre of the tank, as pointed by the arrows in Fig. 4. Just above the impeller, a conic zone with lower gas is found and it extends axially up to 0.39D above the plane of the impeller, highlighted by the red triangle in Fig. 4. These qualitative behaviors are adopted together with the quantitative results presented in this section, to validate the computational simulations results in the following section.

5.2. *Numerical Simulations Results*

5.2.1. *Preliminary results and effect of the modelling set-up*

Before coupling the solution of the PBM with the flow equations, preliminary studies were performed. In particular, the grid influence on the single-phase results was tested, together with the effect of the domain height and the approach to describe the impeller rotation on the gas distribution.

The impeller power consumption in single-phase was calculated by measuring the torque on the moving walls, the torque on the fixed walls and the mass integral of the turbulent dissipation rate in the whole liquid volume. The ungassed power number was calculated with Eq. (24), and the power number from the torque on the moving and fixed walls is equal to 5.15 and 5.14, respectively, in very good agreement with the experimental value of 5.16. The power number obtained from the mass integral of the turbulent dissipation rate in the whole volume is equal to 4.70, which is just 9.0% lower than the experimental value. The turbulence dissipation rate affects the predictions of the PBM kernels since both the breakup and coalescence rate increase with this variable. Therefore, the turbulent dissipation rate in the impeller zone was calculated and compared with its Richardson extrapolation, ε_{RE}, obtained in a previous work (Maluta et al., 2021a). The non dimensional Richardson extrapolation of the average turbulent dissipation rate in the volume swept by the impeller, ε^*_{RE}, is defined as:

$$\varepsilon^*_{RE} = \varepsilon_{RE}/D^2N^3 \quad (25)$$

and it is equal to 7.97, which is just 3.9% higher than the value obtained with the current mesh, which is equal to 7.66. A closer agreement may be obtained by increasing the number of cells in the domain, at the expenses of larger computational times.

The effect of the tank height was successively addressed. For this study, gas-liquid simulations with a constant bubble diameter obtained from the correlation by Alves (Alves et al., 2002) were run. The velocity and gas volume fraction profiles as predicted by the different simulations are almost perfectly overlapping, as shown by means of example in Fig. 5.

Fig. 5 shows that the height of the tank has negligible effects on the results by the simulations. The height of the tank equal to 2 T was studied since at high gas hold-ups the liquid level may change due to the dispersed gas volume fraction, and a constant liquid level may not be representative of the system. In the present work the two different tank heights were considered to highlight whether or not the different modelling approach affects the results, even though the variation of the liquid height is around few millimeters and cannot be experimentally measured. The analysis may serve as a preliminary result to model aerated stirred tank at higher gas hold-ups, where the liquid variation due to the dispersed gas volume fraction is higher.

In the following, a tank height equal to 2 T with a liquid height of 1.4 T was considered in the study, to better replicate the experimental conditions.

5.2.2. *Bubble size distribution*

The bubble size distributions obtained by the different breakup models are compared with the experimental results presented in Section 5.1. The experimental and numerical PDFs are shown in Fig. 6 together with the numerical results obtained from the solution of the PBM with QMOM.

The quadrature method of moments produces local sets of the first 6 moments of the number density function. Applying the product-difference moment inversion algorithm, the six moments are converted in 3 abscissas and 3 weights, and their mass average in the sampling zones are shown in Fig. 6. The same data treatment is adopted to obtain the experimental abscissa and weights. In both the sampling locations the distributions obtained from the

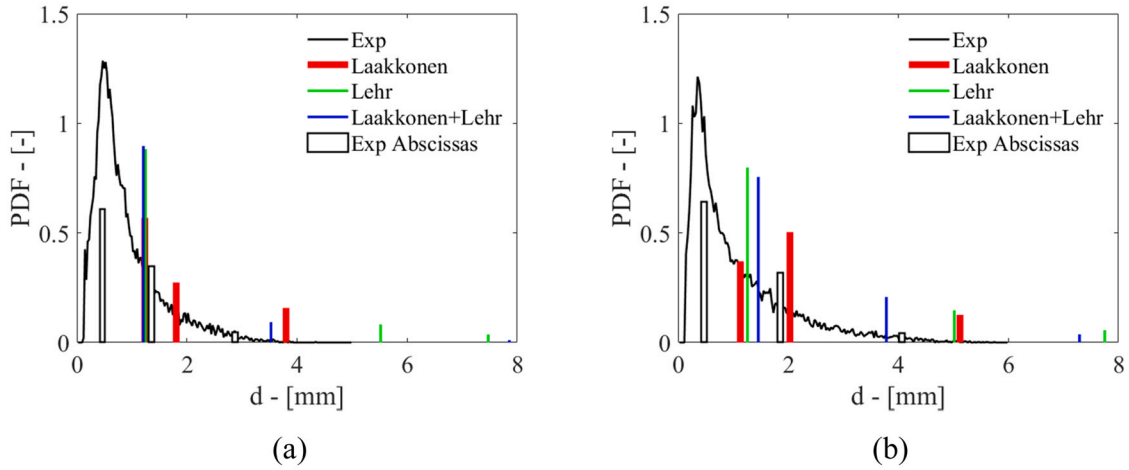

Fig. 6 – Experimental PDFs, experimental abscissas and numerical abscissas from the PBM with different breakup kernels for the lower (a) and the upper (b) measurement location.

numerical solution of the PBM are shifted towards larger bubble sizes, with respect to the experimental distributions. In the lower measurement location, Fig. 6a, the breakup model by Laakkonen et al. (Laakkonen et al., 2006) better describes the experimental distribution, but overpredicts the amount of larger bubbles. The same trend is observed with the Lehr breakup kernel (Lehr et al., 2002) and with the kernel adopting the breakup rate of Laakkonen and the daughter distribution function proposed by Lehr. These two latter kernels, in particular, predict a distribution with bubble sizes larger than 5 mm, which are not observed in the experiments. In the upper measurement position, Fig. 6b, the simulation with the breakup kernel by Laakkonen predict a shape of the PDF that largely deviates from the experimental observations. The other two models, on the other hand, exhibit the same behavior noticed in the lower measurement zone, predicting bubble sizes larger than 6 mm, which are not present in the experimental PDFs.

The mean diameters predicted by the different simulations are compared with the experimental mean diameters in the two different sampling zones, and they are reported in Fig. 7 together with the experimental values.

The deviations between the numerical, d^{CFD}, and experimental, d^{EXP}, diameters were calculated as:

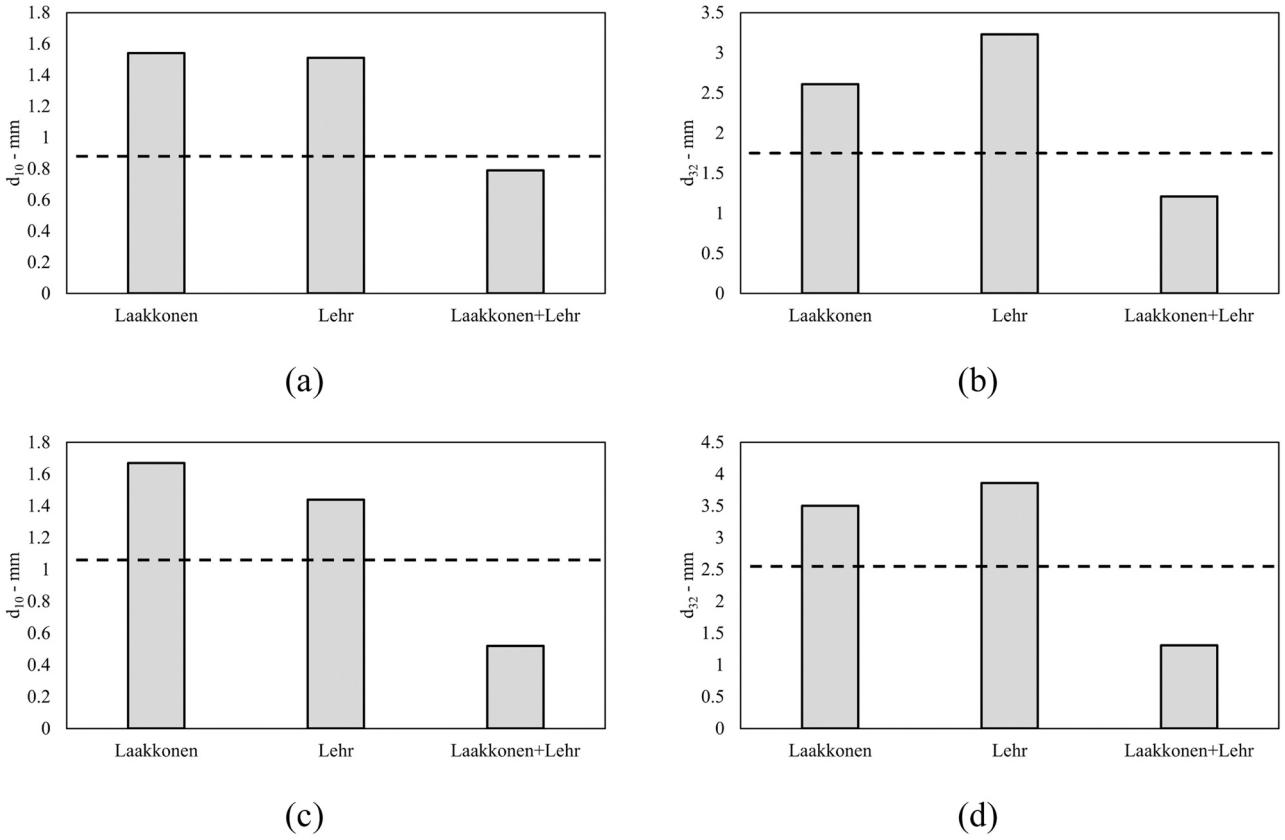

Fig. 7 – Numerically predicted d_{10} (a-c) and d_{32} (b-d) in the lower (a-b) and upper (c-d) measurement positions (bars) and the corresponding experimental value (dashed lines).

Table 2 – Experimental mean diameters and their deviations from the corresponding experimental mean diameters.

	Lower Position		Upper Position	
	d_{10} Δ_{EXP}	d_{32} Δ_{EXP}	d_{10} Δ_{EXP}	d_{32} Δ_{EXP}
Laakkonen	74.5%	48.6%	57.6%	37.4%
Lehr	71.4%	84.1%	35.2%	51.6%
Laakkonen+Lehr	-10.4%	-31.0%	-50.9%	-48.4%

$$\Delta_{EXP} = \frac{d^{CFD} - d^{EXP}}{d^{EXP}} \times 100 \quad (26)$$

and they are reported in Table 2.

Fig. 7 and Table 2 show that both the Laakkonen and the Lehr kernels overpredict the mean diameters in both measurement locations. On the other hand, the kernel adopting the breakup rate by Laakkonen and the DDF by Lehr underpredicts the mean diameters. The adoption of the Laakkonen breakup kernel leads to overall better predictions of the Sauter mean diameter with respect to the d_{10}, as shown by the lower deviations. Conversely, the breakup kernel by Lehr performs slightly better in the prediction of the d_{10}. Adopting the combination of the Laakkonen and Lehr breakup kernels slightly improves the agreement with the experimental data. The experimental trend of increasing bubble mean diameters from the lower to the upper measurement zone is correctly captured just with the adoption of the Laakkonen kernel (Fig. 7), while the other two kernels predict a decreasing trend for the d_{10}, while correctly reproducing the increasing trend for the d_{32}. It can be deduced that the daughter distribution function proposed by Lehr produces too many small daughter bubbles that are known to affect the numerical average bubble diameter more than the Sauter mean diameter.

5.2.3. *Aerated cavities and Relative Power Demand*

All the different numerical simulations, including the simulation with a constant bubble diameter, predicted the aerated cavities forming behind the blades of the impeller, and they are shown in Fig. 8. Fig. 8 shows the region in the impeller in which the gas volume fraction is higher than 0.95, which is a threshold value adopted to identify the aerated cavities (Maluta et al., 2021c, 2021d). Fig. 8 also shows that the simulations with the breakup kernels by Laakkonen, Fig. 8a, and Lehr, Fig. 8b, correctly predict the shape of the '3–3' aerated cavities experimentally observed and shown in Fig. 3. The simulation with the combination of the Laakkonen and Lehr breakup kernels, Fig. 8c, does not predict the alternating pattern of large and clinging cavities. From the simulation with a constant bubble diameter equal to the Sauter mean diameter predicted by the correlation by Alves, Fig. 8d, the '3–3' cavities are obtained.

The ratio between the projected area of the cavities and the projected area swept by the impeller was calculated for all simulations, analogously to what it was done for the experimental measurement, and the results are shown in Fig. 9.

The simulations with the breakup kernels by Laakkonen and Lehr predict a dimensionless cavity size equal to 0.42 and 0.45, respectively. Both simulations slightly overpredict the dimension of the cavities, since the experimental projected area ratio is equal to 0.36, but given the uncertainties

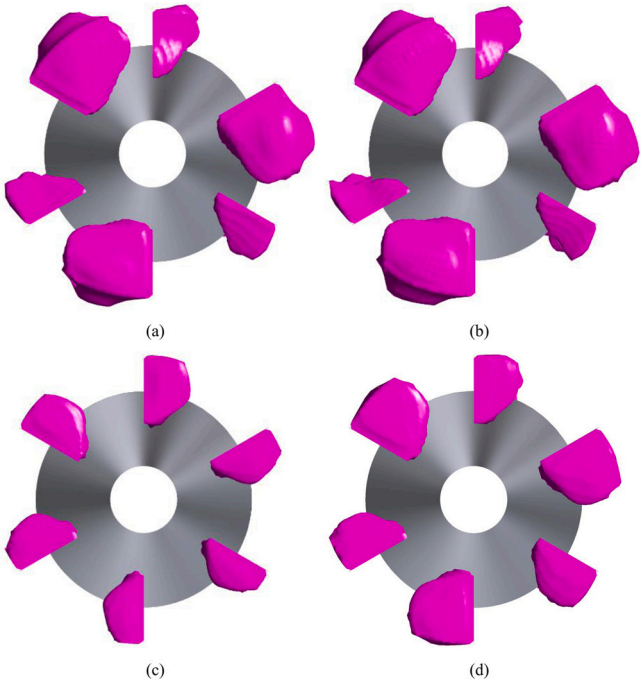

Fig. 8 – Bottom view of the impeller with aerated cavities behind the blades of the impeller (in pink) as predicted by the CFD simulations adopting the Laakkonen (a), the Lehr (b), the combination of the Laakkonen and Lehr (c) breakup kernels and the simulation with constant bubble diameter (d).

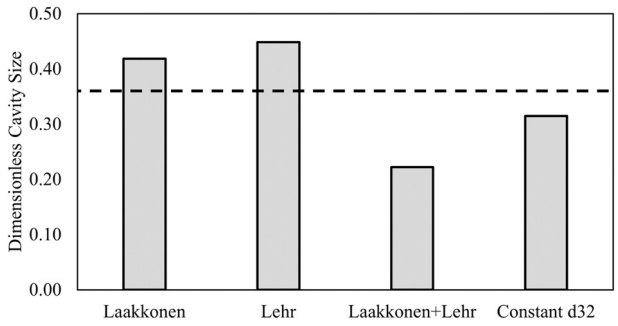

Fig. 9 – Ratio between the projection on a horizontal plane of the cavity area and the impeller swept area, as predicted by the different simulations (bars) and the experimental value (dashed line).

in the definition of the gas volume fraction threshold and in the experimental measurements, overall, an acceptable agreement is found. From the simulation with the combination of the two breakup kernels, a ratio of cavity and swept impeller projected areas equal to 0.22 is obtained, meaning that the simulation underpredicts the size of the cavities. The simulation with a constant bubble size gives a ratio of the projected cavity area to the swept area equal to 0.31, thus slightly underpredicting the experimental cavity size. The prediction of the aerated cavities obtained with a single bubble diameter in different operative conditions was thoroughly addressed and analyzed in a previous work (Maluta et al., 2021d). A good agreement with experimental data was found when the adopted bubble size represents the Sauter mean diameter in the impeller zone. The importance of the bubble size in the impeller zone and the current limits in its

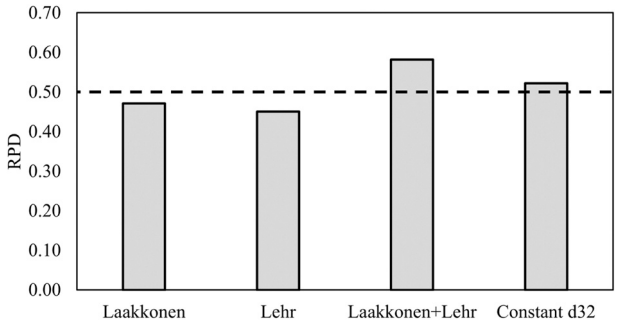

Fig. 10 – RPD as predicted by the different numerical simulations (bars) and the experimental value (dashed line).

prediction by some of the most adopted PBM kernels were also previously discussed (Maluta et al., 2022b). For these reasons, it can be inferred that the PBM kernels play a crucial role in correctly predicting the size and shape of the aerated cavities.

Since the first pioneering work on aerated stirred tanks (Nienow, 1990; Nienow et al., 1985; Warmoeskerken et al., 1981), it is known that the size of the cavities affects the impeller power consumption. The RPDs predicted by the different simulations is shown in Fig. 10.

Fig. 10 shows that with the breakup rate by Laakkonen and Lehr the RPDs are equal to 0.47 and 0.45, respectively, while the simulation with the combination of the two breakup kernels gives a RPD equal to 0.58. This result is coherent with the analysis on the size of the aerated cavities, since larger cavities produce a lower RPD. Therefore, the two simulations with the kernels by Laakkonen and Lehr almost match the experimental RPD, which is equal to 0.50. The simulation with a constant bubble size gives the best prediction of the RPD, which is 0.52, coherently with the results of Fig. 9, where this simulation predicted the best agreement of the cavity size with the experimental data.

In a previous work, it was shown that the bubble terminal velocity in the impeller volume largely affects the calculated size of the cavities and the RPD (Maluta et al., 2021d). The mass average Sauter mean diameter in the volume swept by the impeller is shown in Table 3, together with the Sauter mean diameter predicted by the correlation by Alves (Alves et al., 2002), and the corresponding terminal velocities predicted by Eq. (8).

Table 3 shows that the adoption of the breakup kernel that combines the Laakkonen and the Lehr model predicts a diameter in the impeller swept volume closer to the prediction by the correlation by Alves, while the other two simulations overpredict this value. Despite the large difference in the predicted bubble size from the simulations with the Laakkonen and the Lehr breakup kernel, the resulting terminal velocity is comparable. In a previous work (Maluta et al., 2021d), it was shown that the size of the cavities changes slightly with the bubble size in the impeller zone, when this is larger than about 2 mm. This explains why the cavities and the RPD between the two simulations are similar.

The simulation with a constant bubble size compared to the simulation with the combination of the Laakkonen and Lehr breakup kernel confirms that small differences in the bubble terminal velocity in the impeller zone gives rise to appreciable differences in the gas accumulation in the impeller zone, when the bubble size in the impeller zone is smaller than around 2 mm.

5.2.4. *Gas volume fraction distribution*

Lastly, the gas volume fraction distribution in the tank was calculated, and it is shown in Fig. 11.

The simulations with the Laakkonen, Fig. 11a, and Lehr, Fig. 11b, breakup kernels predict similar gas volume fraction distributions. In particular, in both simulations the vertical motion of the bubbles deviates towards the centre of the tank at about $z/T \approx 1$, as also predicted by the other two modelling approaches shown in Fig. 11c and Fig. 11d. The simulations with the Laakkonen and Lehr breakup kernel predict almost no bubbles recirculating below the plane of the impeller and the discharge jet from the impeller forms an angle of about 24° with the plane of the impeller. One small but noticeable difference is in the size of the zone devoid of bubbles found above the plane of the impeller at low radial coordinates. This zone extends above the plane of the impeller up to 0.65D in Fig. 11a and up to 0.71D in Fig. 11b, and both values are larger than the experimental observation of 0.39D. In Fig. 11c and Fig. 11d the results of the simulations obtained with the combination of the two breakup kernels and the simulation with a constant bubble diameter are presented. In these simulations the bubble terminal velocity in the impeller zone was much smaller than what predicted by the Laakkonen and Lehr models, confirming once again the importance of this parameter in the prediction of the gas-liquid fluid dynamics. In Fig. 11c the gas phase reaches the bottom of the tank, differing from the experimental observations, while in the simulation with a constant bubble diameter the gas phase is found just up to $z/T \approx 0.11$. This value is lower than the one experimentally observed, but the correct trend is predicted by the simulation. The jet radially discharged by the impeller forms an angle of approximately 16° in Fig. 11c and of 17° in Fig. 11d, improving the agreement with the experimental data, with respect to the simulations which adopted the Laakkonen and Lehr breakup rate. The simulation with the combination of the Laakkonen and Lehr breakup rate does not predict a zone with lower gas volume fraction just above the impeller plane, while the simulation with a constant bubble diameter does. This zone extends up to 0.34D above the plane of the impeller, just slightly underestimating the experimental extension by about 14%.

The breakup model by Laakkonen includes 3 empirical parameters that were tuned in different operative conditions in terms of impeller rotational speed, aeration rate and tank size. In particular, aeration rates ranging from 0.018vvm to 0.1vvm were investigated, which are substantially lower than

Table 3 – Sauter mean diameter in the volume swept by the impeller as predicted by the different simulations and by the correlation by Alves. The corresponding terminal velocity are also shown.

	Laakkonen	Lehr	Laakkonen+Lehr	Alves Correlation
d_{32} [mm]	2.24	5.89	1.12	1.28
Ut [cm/s]	21.3	23.9	13.0	14.5

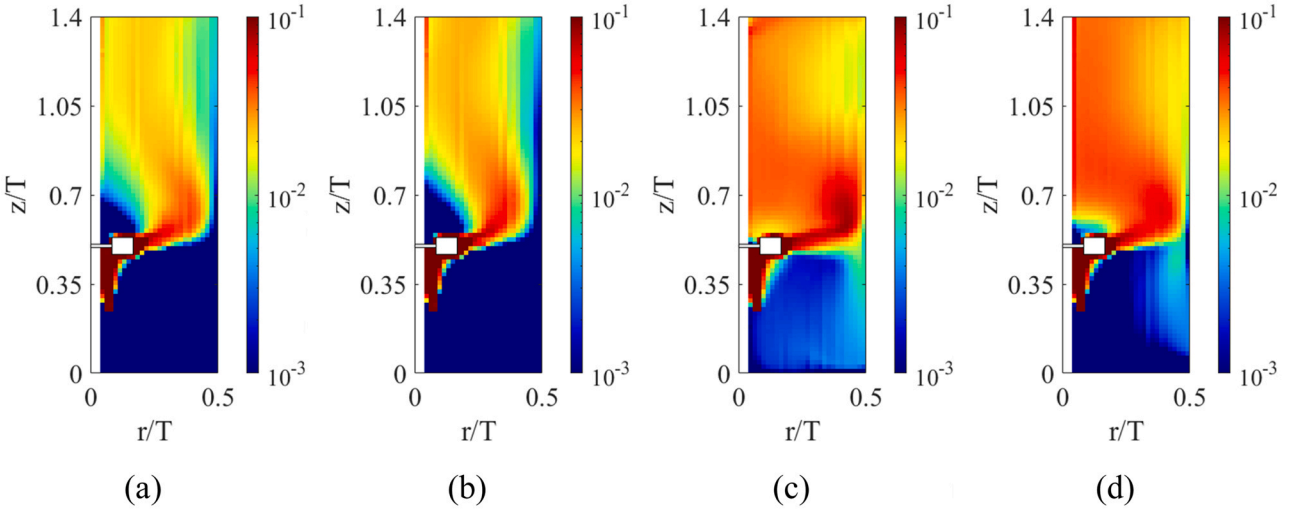

Fig. 11 – Circumferential average of gas volume fraction distribution as predicted by the simulations with the Laakkonen (a), Lehr (b) and the combination of the Laakkonen and Lehr (c) breakup kernels and with the constant bubble diameter (d).

the aeration rate considered in this work and equal to 0.73vvm (Laakkonen et al., 2006). Notably, the parameter C_2 cannot reliably be predicted a priori and it requires fitting procedures based on experimental data in several conditions to be determined (Petitti et al., 2010). Based on the present results, increasing the value of C_2 improves the agreement of the simulations predictions obtained with the breakup model by Laakkonen, while decreasing it improves the agreement of the simulation with the combination of the breakup kernel by Laakkonen and Lehr. It must be emphasized that the empirical parameters in the kernels may even be dependent on the computational grid size, and especially on the grid resolution adopted to fit the parameters values from experiments (Maluta et al., 2021a). While performing a parameter fitting, the grid resolution must be considered, since effects due to the physical phenomena and numerical aspects may contribute to the final bubble size distribution. The breakup model proposed by Lehr does not have adjustable empirical constants. It was developed to predict the bubble size distribution in bubble columns. This model has been previously adopted in the simulation of aerated stirred tanks at low gas flow rates (Kálal et al., 2014b; Laakkonen et al., 2007) with relatively poor results. Being solely based on first principles with no adjustable parameters, and since the gas flow rate in the present work is substantially higher than those previously studied, the breakup model by Lehr may have been appealing, but evidently some of its underlining physical principles may be not directly transferrable to aerated stirred tanks.

The tuning of the kernel parameters is outside the scope of the present work, but it could be addressed in the future, based on the presented data.

6. Conclusion

The investigation of the air sparged tank stirred with a Rushton turbine at aeration rates and power consumption similar to those typically adopted in fermentation processes provided the following main observations:

- the bubble size distributions in two measurement zones located above the impeller exhibit very similar features;
- the BSD obtained from simulations with the breakup kernel by Laakkonen, by Lehr, and by a combination of the two models showed that bubbles with sizes larger than what experimentally observed are predicted;
- the kernels by Laakkonen and Lehr overpredict the mean diameters of the distribution, while the combination of the two kernels underestimates them;
- the shape of the aerated cavities experimentally observed is better replicated by the adoption of the kernels by Laakkonen and Lehr, while the combination of the two models fails in predicting the '3–3' cavity structure;
- the size of the aerated cavities obtained with the constant bubble size in the impeller zone as predicted by the correlation by Alves better agrees with the experimental data, while the two kernels by Laakkonen and Lehr overestimate this size and conversely the combination of the two models underestimates it. The same trend is unsurprisingly observed in the relative power demand;
- the numerical gas volume fraction distributions qualitatively agree with the experimental observation, with the simulation with a constant bubble diameter in slightly better agreement than the simulations coupled with the PBM.

Overall, the predictions with the kernels analyzed in this study only show a partial agreement with the experimental measurements, highlighting once again the importance of correctly predicting the bubble size in the impeller zone. This may be due both to an intrinsic limit of the models in the operative conditions considered, which consider a higher gas flow rate than what used to derive and test them, and to the set of empirical constants of the model, which may need fitting to describe different operative conditions. A possible dependence of the kernel parameters on the computational grid, as observed in liquid-liquid systems, should be investigated to improve the predictive capabilities of such models.

Declaration of Competing Interest

The authors declare that they have no known competing financial interests or personal relationships that could have appeared to influence the work reported in this paper.

Acknowledgments

The experimental and computational investigations carried out in this and many other works of the Mixing group at Unibo are guided from the firm achievements of Professor Alvin W. Nienow. We will always keep the memory of his scientific guidance and friendship.

References

Alves, S.S., Maia, C.I., Vasconcelos, J.M.T., Serralheiro, A.J., 2002. Bubble size in aerated stirred tanks. Chem. Eng. J. 89, 109–117. https://doi.org/10.1016/S1385-8947(02)00008-6

Aubin, J., Le Sauze, N., Bertrand, J., Fletcher, D.F., Xuereb, C., 2004. PIV measurements of flow in an aerated tank stirred by a down- and an up-pumping axial flow impeller. Exp. Therm. Fluid Sci. 28, 447–456. https://doi.org/10.1016/j.expthermflusci.2001.12.001

Bakker, A., Van den Akker, H.E.A., 1994. Computational model for the gas-liquid flow in stirred reactors. Chem. Eng. Res. Des. 72, 594–606.

Balachandar, S., Eaton, J.K., 2010. Turbulent dispersed multiphase flow. Annu Rev. Fluid Mech. 42, 111–133. https://doi.org/10.1146/annurev.fluid.010908.165243

Bruijn, W., van't Riet, K., Smith, J.M., 1974. Power consumption with aerated Rushton turbines. Trans. Inst. Chem. Eng. 52, 88–104.

Buffo, A., Marchisio, D.L., 2014. Modeling and simulation of turbulent polydisperse gas-liquid systems via the generalized population balance equation. Rev. Chem. Eng. 30, 73–126. https://doi.org/10.1515/revce-2013-0015

Buffo, A., Marchisio, D.L., Vanni, M., Renze, P., 2013. Simulation of polydisperse multiphase systems using population balances and example application to bubbly flows. Chem. Eng. Res. Des. 91, 1859–1875. https://doi.org/10.1016/j.cherd.2013.06.021

Buffo, A., Vanni, M., Marchisio, D.L., 2016. On the implementation of moment transport equations in OpenFOAM: boundedness and realizability. Int. J. Multiph. Flow. 85, 223–235. https://doi.org/10.1016/j.ijmultiphaseflow.2016.06.017

Buffo, A., Vanni, M., Marchisio, D.L., 2012. Multidimensional population balance model for the simulation of turbulent gas–liquid systems in stirred tank reactors. Chem. Eng. Sci. 70, 31–44. https://doi.org/10.1016/j.ces.2011.04.042

Burns, A.D., Frank, T., Hamill, I., Shi, J.-M.M., 2004. The Favre Averaged Drag Model for Turbulent Dispersion in Eulerian Multi-Phase Flows, in: Fifth International Conference on Multiphase Flow, ICMF-2004. Yokohama, Japan, pp. 1–17.

Busciglio, A., Grisafi, F., Scargiali, F., Brucato, A., 2013. On the measurement of local gas hold-up, interfacial area and bubble size distribution in gas–liquid contactors via light sheet and image analysis: Imaging technique and experimental results. Chem. Eng. Sci. 102, 551–566. https://doi.org/10.1016/j.ces.2013.08.029

Cappello, V., Plais, C., Vial, C., Augier, F., 2021. Scale-up of aerated bioreactors: CFD validation and application to the enzyme production by Trichoderma reesei. Chem. Eng. Sci. 229, 116033. https://doi.org/10.1016/j.ces.2020.116033

Chapman, C.M., Gibilaro, L.G., Nienow, A.W., 1982. A dynamic response technique for the estimation of gas—liquid mass transfer coefficients in a stirred vessel. Chem. Eng. Sci. 37, 891–896. https://doi.org/10.1016/0009-2509(82)80177-2

Clift, R., Grace, J.R., Weber, M.E., 2005. Bubbles, drops, and particles, 1st ed. Dover Publications, Inc, Mineola, New York.

Coulaloglou, C.A., Tavlarides, L.L., 1977. Description of interaction processes in agitated liquid-liquid dispersions. Chem. Eng. Sci. 32, 1289–1297. https://doi.org/10.1016/0009-2509(77)85023-9

Dantec Dynamics, 2022. DynamicStudio User's Guide.

Fdida, N., Blaisot, J.-B., 2010. Drop size distribution measured by imaging: determination of the measurement volume by the calibration of the point spread function. Meas. Sci. Technol. 21, 025501. https://doi.org/10.1088/0957-0233/21/2/025501

Hasan, B.O. Experimental study on the bubble breakage in a stirred tank. Part 1. Mechanism and effect of operating parameters. International Journal of Multiphase Flow 97, 94–108. https://doi.org/10.1016/j.ijmultiphaseflow.2017.08.006.

Hassan, I.T.M., Robinson, C.W., 1977. Stirred-tank mechanical power requirement and gas holdup in aerated aqueous phases. AIChE J. 23, 48–56. https://doi.org/10.1002/aic.690230109

Howarth, W.J., 1964. Coalescence of drops in a turbulent flow field. Chem. Eng. Sci. 19, 33–38. https://doi.org/10.1016/0009-2509(64)85003-X

K. Van't Riet, 1976. Turbine agitator Hydrodynamics and dispersion performance. University of Delft, Delft, The Netherlands.

Kálal, Z., Jahoda, M., Fořt, I., 2014a. CFD prediction of gas-liquid flow in an aerated stirred vessel using the population balance model. Chem. Process Eng. 35, 55–73. https://doi.org/10.2478/cpe-2014-0005

Kálal, Z., Jahoda, M., Fořt, I., 2014b. Modelling of the bubble size distribution in an aerated stirred tank: theoretical and numerical comparison of different breakup models. Chem. Process Eng. 35, 331–348. https://doi.org/10.2478/cpe-2014-0025

Laakkonen, M., Alopaeus, V., Aittamaa, J., 2006. Validation of bubble breakage, coalescence and mass transfer models for gas–liquid dispersion in agitated vessel. Chem. Eng. Sci. 61, 218–228. https://doi.org/10.1016/j.ces.2004.11.066

Laakkonen, M., Moilanen, P., Alopaeus, V., Aittamaa, J., 2007. Modelling local bubble size distributions in agitated vessels. Chem. Eng. Sci. 62, 721–740. https://doi.org/10.1016/J.CES.2006.10.006

Laakkonen, M., Moilanen, P., Miettinen, T., Saari, K., Honkanen, M., Saarenrinne, P., Aittamaa, J., 2005. Local bubble size distributions in agitated vessel: comparison of three experimental techniques. Chem. Eng. Res. Des. 83, 50–58. https://doi.org/10.1205/cherd.04122

Lehr, F., Millies, M., Mewes, D., 2002. Bubble-Size distributions and flow fields in bubble columns. AIChE J. 48, 2426–2443. https://doi.org/10.1002/aic.690481103

Leibson, I., Holcomb, E.G., Cacoso, A.G., Jacmic, J.J., 1956. Rate of flow and mechanics of bubble formation from single submerged orifices. I. Rate of flow studies. AIChE J. 2, 296–300. https://doi.org/10.1002/aic.690020305

Liao, Y., Lucas, D., 2009. A literature review of theoretical models for drop and bubble breakup in turbulent dispersions. Chem. Eng. Sci. 64, 3389–3406. https://doi.org/10.1016/j.ces.2009.04.026

Liao, Y., Lucas, D., 2010. A literature review on mechanisms and models for the coalescence process of fluid particles. Chem. Eng. Sci. 65, 2851–2864. https://doi.org/10.1016/j.ces.2010.02.020

Linek, V., Beneš, P., Vacek, V., Hovorka, F., 1982. Analysis of differences in kℓa values determined by steady-state and dynamic methods in stirred tanks. Chem. Eng. J. 25, 77–88. https://doi.org/10.1016/0300-9467(82)85024-7

Maluta, F., Paglianti, A., Montante, G., 2019. Modelling of biohydrogen production in stirred fermenters by computational fluid dynamics. Process Saf. Environ. Prot. 125, 342–357. https://doi.org/10.1016/j.psep.2018.09.020

Maluta, F., Buffo, A., Marchisio, D., Montante, G., Paglianti, A., Vanni, M., 2021a. Effect of turbulent kinetic energy dissipation rate on the prediction of droplet size distribution in stirred tanks. Int. J. Multiph. Flow. 136, 103547. https://doi.org/10.1016/j.ijmultiphaseflow.2020.103547

Maluta, F., Buffo, A., Marchisio, D., Montante, G., Paglianti, A., Vanni, M., 2021b. Numerical and experimental analysis of the daughter distribution in liquid-liquid stirred tanks. Chem. Eng. Technol. 44, 1994–2001. https://doi.org/10.1002/ceat.202100237

Maluta, F., Paglianti, A., Montante, G., 2021c. Two-fluids RANS predictions of gas cavities, power consumption, mixing time

and oxygen transfer rate in an aerated fermenter scale-down stirred with multiple impellers. Biochem Eng. J. 166, 107867. https://doi.org/10.1016/j.bej.2020.107867
Maluta, F., Paglianti, A., Montante, G., 2021d. Prediction of gas cavities size and structure and their effect on the power consumption in a gas-liquid stirred tank by means of a two-fluid RANS model. Chem. Eng. Sci. 241, 116677. https://doi.org/10.1016/j.ces.2021.116677
Maluta, F., Alberini, F., Montante, G., Paglianti, A., 2022a. Validation of a procedure for the numerical simulations of gas–liquid stirred tanks by means of a computational fluid dynamics approach. Can. J. Chem. Eng. 100, 3472–3485. https://doi.org/10.1002/cjce.24548
Maluta, F., Paglianti, A., Montante, G., 2022b. Towards a CFD-PBE simulation of aerated stirred tanks at high gas hold ups and different flow regimes. Chem. Eng. Res. Des. 180, 425–436. https://doi.org/10.1016/j.cherd.2021.10.018
Maluta, F., Paglianti, A., Montante, G., 2022c. Towards a robust CFD modelling approach for reliable hydrodynamics and mass transfer predictions in aerobic stirred fermenters. Biochem Eng. J. 181, 108405. https://doi.org/10.1016/j.bej.2022.108405
Manikowski, M., Bodemeier, S., Lübbert, A., Bujalski, W., Nienow, A.W., 2009. Measurement of gas and liquid flows in stirred tank reactors with multiple agitators. Can. J. Chem. Eng. 72, 769–781. https://doi.org/10.1002/cjce.5450720502
Marchisio, D.L., Fox, R.O., 2013. Computational Models for Polydisperse Particulate and Multiphase Systems, Cambridge University Press. Cambridge University Press,, Cambridge. https://doi.org/10.1017/CBO9781139016599
Middleton, J.C., Smith, J.M., 2004. Gas-liquid mixing in turbulent systems. In: Paul, E.L., Atiemo-Obeng, V.A., Kresta, S.M. (Eds.), Handbook of Industrial Mixing: Science and Practice. John Wiley & Sons Inc, Hoboken, New Jersey, pp. 585–638.
Montante, G., Horn, D., Paglianti, A., 2008. Gas–liquid flow and bubble size distribution in stirred tanks. Chem. Eng. Sci. 63, 2107–2118. https://doi.org/10.1016/j.ces.2008.01.005
Nienow, A.W., 1990. Gas dispersion performance in fermenter operation. Chem. Eng. Prog. 86, 61–71.
Nienow, A.W., 1998. Hydrodynamics of stirred bioreactors. Appl. Mech. Rev. 51, 3–32. https://doi.org/10.1115/1.3098990
Nienow, A.W., Lilly, M.D., 1979. Power drawn by multiple impellers in sparged agitated vessels. Biotechnol. Bioeng. 21, 2341–2345. https://doi.org/10.1002/bit.260211214
Nienow, A.W., Warmoeskerken, M.M.C.G., Smith, J.M., Konno, M., 1985. On the flooding/loading transition and the complete dispersal condition in aerated vessels agitated by a Rushton-turbine, in: Proc. of the 5th European Conf. on Mixing. BHRA Fluid Engineering, Wurzburg, Germany, pp. 143–154.
Nienow, A.W., Wisdom, D.J.J., Middleton, J.C., 1977. The effect of scale and geometry on flooding, recirculation, and power in gassed stirred vessels. Proc. 2nd European Mixing Conference F1–1-F1–16.
Niño, L., Gelves, R., Ali, H., Solsvik, J., Jakobsen, H., 2020. Applicability of a modified breakage and coalescence model based on the complete turbulence spectrum concept for CFD simulation of gas-liquid mass transfer in a stirred tank reactor. Chem. Eng. Sci. 211, 115272. https://doi.org/10.1016/j.ces.2019.115272
Paglianti, A., Fujasova, M., Montante, G., 2008. A simple model for power consumption in gassed and boiling stirred vessels. AIChE J. 54, 646–656. https://doi.org/10.1002/aic.11414
Petitti, M., Nasuti, A., Marchisio, D.L., Vanni, M., Baldi, G., Mancini, N., Podenzani, F., 2010. Bubble size distribution modeling in stirred gas-liquid reactors with QMOM augmented by a new correction algorithm. AIChE J. 56, 36–53. https://doi.org/10.1002/aic.12003
Petitti, M., Vanni, M., Marchisio, D.L., Buffo, A., Podenzani, F., 2013. Simulation of coalescence, break-up and mass transfer in a gas–liquid stirred tank with CQMOM. Chem. Eng. J. 228, 1182–1194. https://doi.org/10.1016/j.cej.2013.05.047
Pinelli, D., Bujalski, W., Nienow, A.W., Magelli, F., 2001. Comparison of experimental techniques for the measurement of mixing time in gas-liquid systems. Chem. Eng. Technol. 24, 919–923. https://doi.org/10.1002/1521-4125(200109)24:9<919::AID-CEAT919>3.0.CO;2-U
Podgórska, W., Bałdyga, J., 2001. Scale-up effects on the drop size distribution of liquid–liquid dispersions in agitated vessels. Chem. Eng. Sci. 56, 741–746. https://doi.org/10.1016/S0009-2509(00)00284-0
Prince, M.J., Blanch, H.W., 1990. Bubble coalescence and break-up in air-sparged bubble columns. AIChE J. 36, 1485–1499. https://doi.org/10.1002/aic.690361004
Ross, S.L., Curl, R.L., 1973. Measurements and Models of the Dispersed Phase Mixing Process, in: Joint Chem Eng Conf. Vancouver, p. 29b.
Scargiali, F., D'Orazio, A., Grisafi, F., Brucato, A., 2007. Modelling and simulation of gas–liquid hydrodynamics in mechanically stirred tanks. Chem. Eng. Res. Des. 85, 637–646. https://doi.org/10.1205/cherd06243
Sideman, Samuel, Hortaçsu, Öner, Fulton, J.W., 1966. Mass transfer in gas-liquid contacting systems. Ind. Eng. Chem. 58, 32–47. https://doi.org/10.1021/ie50679a006
Simonnet, M., Gentric, C., Olmos, E., Midoux, N., 2007. Experimental determination of the drag coefficient in a swarm of bubbles. Chem. Eng. Sci. 62, 858–866. https://doi.org/10.1016/j.ces.2006.10.012
Smith, J.M., Van't Riet, K., Middleton, J.C, 1977. Scale up of agitated gas–liquid reactors for mass transfer, in: Proceedings of 2nd European Conference on Mixing. Mons, BE, pp. 51–66.
Smith, J.M., Warmoeskerken, M.M.C.G., Zeef, E., 1987. Flow conditions in vessels dispersing gases in liquids with multiple impellers. In: Ho, C.S., Oldshue, J.Y. (Eds.), Biotechnology Processes: Scale-up and Mixing. American Institute of Chemical Engineers, New York, pp. 107–115.
Solsvik, J., Jakobsen, H.A., 2015. Single Air Bubble Breakup Experiments in Stirred Water Tank. Int. J. Chem. React. Eng. 13, 477–491. https://doi.org/10.1515/ijcre-2014-0154
Solsvik, J., Tangen, S., Jakobsen, H.A., 2013. On the constitutive equations for fluid particle breakage. Rev. Chem. Eng. 29, 241–356. https://doi.org/10.1515/revce-2013-0009
Takahashi, K., McManamey, W.J., Nienow, A.W., 1992. Bubble size distributions in impeller region in a gas-sparged vessel agitated by a Rushton turbine. J. Chem. Eng. Jpn. 25, 427–432. https://doi.org/10.1252/jcej.25.427
Takahashi, K., Nienow, A.W., 1992. Vortex cavity shape and the associated path-line of discharged bubbles in an aerated vessel agitated by a Rushton turbine. J. Chem. Eng. Jpn. 25, 539–543. https://doi.org/10.1252/jcej.25.539
Vasconcelos, J.M.T., Nienow, A.W., Martin, T., Alves, S.S., McFarlane, C.M., 1997. Alternative Ways of Applying the Hydrogen Peroxide Steady State Method of KLa Measurement. Chem. Eng. Res. Des. 75, 467–472. https://doi.org/10.1205/026387697523967
Venneker, B.C.H., Derksen, J.J., Van den Akker, H.E.A., 2002. Population balance modeling of aerated stirred vessels based on CFD. AIChE J. 48, 673–685. https://doi.org/10.1002/aic.690480404
Vonka, M., Soos, M., 2015. Characterization of liquid-liquid dispersions with variable viscosity by coupled computational fluid dynamics and population balances. AIChE J. 61, 2403–2414. https://doi.org/10.1002/aic.14831
Wang, H., Felis, F., Tomas, S., Anselmet, F., Amielh, M., 2017. An improved image processing method for particle characterization by shadowgraphy, in: Proceedings ILASS–Europe 2017. 28th Conference on Liquid Atomization and Spray Systems. Universitat Politècnica València, Valencia, pp. 1–6. https://doi.org/10.4995/ILASS2017.2017.4614
Warmoeskerken, M.M.C.G., Feijen, J., Smith, J.M., 1981. Hydrodynamics and power consumption in stirred gas-liquid dispersions. In: Fluid mixing symposium. Institution of Chemical Engineers, Bradford, U.K., pp. J1–B14.
Warmoeskerken, M.M.C.G., Smith, J.M., 1986. Flow regime maps for Rushton turbines, in: 3rd World Congress of Chemical Engineering. Tokyo.